



Adaptive Lissajous scanning pattern design by phase modulation

DAVID BRUNNER,*  HAN WOONG YOO, RICHARD SCHROEDTER, AND GEORG SCHITTER

TU Wien, Automation and Control Institute (ACIN), Gusshausstrasse 27-29, 1040 Vienna, Austria

*brunner@acin.tuwien.ac.at

Abstract: This paper proposes a phase modulation method for Lissajous scanning systems, which provides adaptive scan pattern design without changing the frame rate or the field of view. Based on a rigorous analysis of Lissajous scanning, phase modulation constrains and a method for pixel calculation are derived. An accurate and simple metric for resolution calculation is proposed based on the area spanned by neighboring pixels and used for scan pattern optimization also considering the scanner dynamics. The methods are implemented using MEMS mirrors for verification of the adaptive pattern shaping, where a 5-fold resolution improvement in a defined region of interest is demonstrated.

Published by The Optical Society under the terms of the [Creative Commons Attribution 4.0 License](https://creativecommons.org/licenses/by/4.0/). Further distribution of this work must maintain attribution to the author(s) and the published article's title, journal citation, and DOI.

1. Introduction

High performance scanning systems aim to traverse a repeating fine grid scan pattern to cover the target field of view (FoV) in a minimum time to achieve fast and high resolution imaging. Considering physical limitations of the scanning devices, those two requirements of speed and spatial resolution are usually contradicting. In environmental perception applications such as lidar for autonomous vehicles a fast reaction on sudden appearing obstacles is safety critical [1,2]. Capturing the whole scene with high resolution might result in a not manageable amount of data and only partly contains useful information. Hence, it can be beneficial to define regions of interest (ROI), which are scanned with a high resolution while the resolution at the rest of the FoV is reduced [3]. This potentially allows a faster frame rate and a lower reaction time as less data overhead is produced. The method can be also used in the manufacturing inspection, where a first overall scan of the inspected device defines region which shall be imaged with higher resolution in a subsequent scan [4,5]. Random access scanning systems can provide such ROI scans as the pixels can be individually addressed.

Inertia free scanning systems based on acousto-optic lenses [6,7] or optical phased arrays [8,9] allow fast random access scanning while the system is complex. Traditional mechanical scanning systems can be generally separated into non-resonant and resonant systems and do not allow true random access scanning as its inertia is finite and the scan speed cannot be changed abruptly. A non-resonant method is the raster scan, where one orthogonal axis is significantly slower than the other to obtain an uniform scan grid. It allows dynamic adjustment of the scan trajectory to perform ROI scans only limited by the necessary bandwidth. This method necessitates a wide control bandwidth considering scanner dynamics to generate multi-harmonic trajectories such as triangle or sawtooth waveforms [10] and is therefore susceptible to noise [11].

A resonant method is Lissajous scanning, where both axes have similar single-tone frequencies whose ratio is a specific rational number. This method allows the scanning system to be operated at resonance to achieve fast and large amplitude scanning, especially with high Q-factors, at a low power consumption. Furthermore, the control design is simple as only a single frequency has to be tracked and therefore usually shows a significantly lower tracking error compared to

#430171

Journal © 2021

<https://doi.org/10.1364/OE.430171>

Received 28 Apr 2021; revised 26 Jul 2021; accepted 27 Jul 2021; published 16 Aug 2021

raster scanning methods [5,11] but provides only low flexibility in scan pattern design. Although Lissajous scanning is much simpler to implement, it generates a non-uniform scan pattern, which only depends on the ratio of both scanning frequencies [11,12]. The pattern resolution is the lowest at the center of the FoV and increases towards the edges, which is typically disadvantageous in applications. A simple metric based on the scan line separation at the center is given in [11] and can be used for scanning frequency selection [13,14]. A universal metric for the spatial resolution based on Voronoi tessellations is used in [15] to optimally select the frequencies also considering the scanner dynamics. A pixel distribution proposed in [16] generates a rectilinear grid by a constant sampling rate, which allows a better processing of the obtained image despite non-uniformity. Dedicated resonant scanners, whose primary operation is at resonance also typically allow a much simpler design and reduced production cost. This assumes that the desired scanning frequency lies in a certain range around the resonance peak, i.e. the resonance bandwidth, which decreases with increasing Q-factor of the system [12]. Not to limit the scanning frequency selection and still achieve high Q-factors, the resonance frequency of a scanning system has to be tunable. Several tuning methods are developed in literature, such as mechanically pre-stressing of the used suspension [5,17] or to change the effective electrostatic stiffness of a micro-electro-mechanical system (MEMS) mirror by manipulating the driving signal [18–20]. A further possibility is to introduce a nonlinear stiffness by using dedicated suspensions, which cause the resonance frequency to depend on the system states, e.g. the amplitude, while the Q-factor can be remained high [21,22]. Considering only a certain tuning range of the scanners, the frame rate usually contradicts with the resolution [13]. A method to obtain effective frame rates higher than the trajectory repetition rate is proposed in [23], where a model-based image reconstruction is used to estimate missing data points.

In this paper a novel method for adaptive Lissajous scanning based on phase modulation is proposed, allowing to shape the scan pattern, e.g. to obtain a ROI, without changing the frame rate. Based on a rigorous analysis of the Lissajous scanning method, design criteria for the phase modulation function and pixel timings are derived. An accurate and simple calculation of the obtained resolution in the full FoV is proposed based on the area spanned by neighboring pixels and subsequently used for scan pattern optimization. The method is demonstrated by two orthogonally oriented single axis resonant MEMS mirrors with enhanced frequency tuning capabilities.

The paper is organized as follows. In Section 2 the terms and notion for conventional Lissajous scanning are introduced and discussed. In Section 3 the phase modulation concept is described. Starting from constraints derivation to pixel distribution and resolution calculation followed by scanning amplitude variation compensation and scan pattern optimization. Section 4 shows a demonstration of the proposed method, providing examples of ROI scans.

2. Preliminaries

A conventional Lissajous scanning pattern is obtained by two single-tone frequencies oscillating along two orthogonal axes X and Y. Hence, the trajectory of both axes can be defined as

$$x(t) = \sin(2\pi f_X t) \quad \text{and} \quad y(t) = \sin(2\pi f_Y t), \quad (1)$$

where f_X and f_Y are the corresponding frequencies. Without loss of generality it is assumed that $f_X > f_Y$ and with $\varphi_X(t) = 2\pi f_X t$ and $\varphi_Y(t) = 2\pi f_Y t$, the evolution of the relative phase can be expressed as

$$\Delta\varphi\left(\frac{N_X}{f_X}\right) = \varphi_X\left(\frac{N_X}{f_X}\right) - \varphi_Y\left(\frac{N_X}{f_X}\right) = 2\pi N_X \cdot \left(1 - \frac{f_Y}{f_X}\right) \quad \text{and} \quad \Delta\varphi\left(\frac{N_Y}{f_Y}\right) = 2\pi N_Y \cdot \left(\frac{f_X}{f_Y} - 1\right), \quad (2)$$

where N_X and N_Y represent the elapsed number of X-axis or Y-axis periods, respectively. The repetition of the Lissajous scan pattern is then defined by the smallest number $K \in \mathbb{N}$ where

$$\Delta\varphi\left(\frac{N_{X0}}{f_X}\right) = \Delta\varphi\left(\frac{N_{Y0}}{f_Y}\right) = 2\pi K, \quad (3)$$

and $N_{X0}, N_{Y0} \in \mathbb{N}$ are the total number of X-axis and Y-axis periods per Lissajous frame. Hence, N_{X0}, N_{Y0} and K can be calculated by the co-prime ratios given as

$$\frac{K}{N_{X0}} = \left(1 - \frac{f_Y}{f_X}\right) \quad \text{and} \quad \frac{K}{N_{Y0}} = \left(\frac{f_X}{f_Y} - 1\right), \quad (4)$$

where $N_{X0} = N_{Y0} + K$ and the period of the Lissajous frame can be calculated to

$$T_0 = \frac{1}{f_0} = \frac{N_{X0}}{f_X} = \frac{N_{Y0}}{f_Y} = \frac{K}{f_X - f_Y}. \quad (5)$$

As an example $f_X = 2392$ Hz and $f_Y = 2366$ Hz are considered, which result in $K = 1$, $N_{X0} = 92$, $N_{Y0} = 91$ and a frame rate $f_0 = 26$ Hz. The resulting resolution of the Lissajous grid is then solely defined by the number of total periods N_{X0} and N_{Y0} where a higher number corresponds to a higher resolution in the respective other axis as shown in Fig. 1. However, due to Eq. (5) a higher number of periods for the Lissajous scan also needs a longer time to repeat, i.e. lowers the frame rate f_0 . The value K defines how fast a preview of the overall scan is provided, which is subsequently filled with scan lines until T_0 . Hence, for $K = 5$ a preview is provided in $T_0/5$ seconds as shown in the figure.

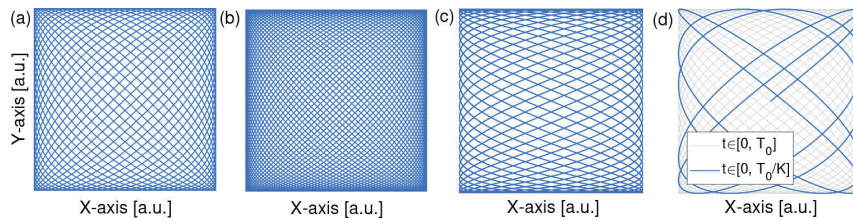


Fig. 1. Examples of Lissajous scan patterns. (a) Low resolution grid ($N_{X0} = 26$, $N_{Y0} = 25$, $K = 1$, $f_0 = 90$ Hz). (b) High resolution grid ($N_{X0} = 46$, $N_{Y0} = 45$, $K = 1$, $f_0 = 52$ Hz). (c) Asymmetric resolution grid ($N_{X0} = 26$, $N_{Y0} = 11$, $K = 15$, $f_0 = 90$ Hz). (d) Fast preview due to $K > 1$ ($N_{X0} = 26$, $N_{Y0} = 21$, $K = 5$, $f_0 = 90$ Hz).

In the case of N_{X0} and N_{Y0} are both odd integers, K is an even value, which results in overlapping scan lines and therefore a reduced resolution. This phenomenon is also discussed in [24], where an initial relative phase shift in Eq. (1) at $t = 0$ is proposed to avoid the overlapping. With the initial phases φ_{X0} and φ_{Y0} for X-axis and Y-axis, the high resolution is recovered if the following condition is met

$$(N_{X0} \varphi_{Y0} - N_{Y0} \varphi_{X0}) = \frac{\pi}{2}. \quad (6)$$

For simplicity, in the following analysis either N_{X0} or N_{Y0} is considered to be even and $\varphi_{X0} = \varphi_{Y0} = 0$, while the case of two odd total period numbers can be analyzed with the same methods.

3. Adaptive Lissajous scanning

In this article a modulation of the relative phase is proposed to shape the Lissajous scan pattern without sacrificing the frame rate and FoV. Hence, the trajectories in Eq. (1) are modified by the

phase modulation function $\phi(t)$ as

$$x(t) = \sin(2\pi f_X t) \quad \text{and} \quad y(t) = \sin(2\pi \bar{f}_Y t + \phi(t)), \quad (7)$$

where \bar{f}_Y is the mean Y-axis frequency and defines the Lissajous scan parameters N_{X0} , N_{Y0} , K and f_0 as given in the previous section. Similarly, the modulation can be applied on the X-axis or both axes.

3.1. Modulation design constraints

By definition, the first constraints of the phase modulation function $\phi(t)$ are

$$\phi(0) = \phi(T_0) = 0, \quad (8)$$

as otherwise the Lissajous trajectory does not repeat after T_0 , resulting in a change of the frame rate or a non-repeating scan. Furthermore, if $K > 1$ the modulation function has to repeat in each preview period T_0/K , which results in the general repetition constraints

$$\phi\left(m \frac{T_0}{K}\right) = 0 \quad \text{and} \quad \phi(t) = \phi\left(m \frac{T_0}{K} + t\right), \quad (9)$$

with any number $m \in \mathbb{Z}$. Without loss of generality the analysis herein assumes the modulation to be fixed for infinite time while in practice the modulation can be changed in subsequent periods. Another constraint can be found by analyzing the anti-symmetry of the first and the second half of a preview period as shown in Fig. 2. For any preview period, the scan line at the first half period starts along the right diagonal and ends along the left diagonal, while the second half period does this vice versa. Hence, to obtain a smooth Lissajous grid the modulation has to be anti-symmetric regarding each preview period, i.e.

$$\phi(t) = -\phi\left(m \frac{T_0}{K} - t\right). \quad (10)$$

This also implies that the modulation function has to be zero at each half of the preview periods. Therefore the necessary constraints, which a phase modulation function has to fulfill can be summarized as

$$\phi\left(m \frac{T_0}{2K}\right) = 0 \quad \text{and} \quad \phi(t) = \phi\left(m \frac{T_0}{K} + t\right) = -\phi\left(m \frac{T_0}{K} - t\right), \quad (11)$$

for any number $m \in \mathbb{Z}$.

The derived constraints in Eq. (11) are automatically fulfilled if the phase modulation function is composed by sine waves with multiple harmonics of the preview frame rate, i.e.

$$\phi(t) = \sum_{i=1}^{\infty} a_i \sin\left(2\pi i \frac{K}{T_0} t\right) = \sum_{i=1}^{\infty} a_i \sin\left(2\pi i (f_X - \bar{f}_Y) t\right), \quad (12)$$

where i is regarded as the modulation order and a_i are the design parameters. The maximum achievable modulation order is practically limited by the scanner dynamics as the frequency of the scanner has to be changed according to the second derivative, i.e. the curvature, of the phase modulation function. Furthermore, to obtain a non-overlapping Lissajous pattern the gradient of the relative phase between both axes has to be positive at any time, resulting in

$$f_X > \bar{f}_Y + \frac{1}{2\pi} \dot{\phi}(t). \quad (13)$$

Figure 3(b)-(d) shows three examples of single order modulation functions, which shape the Lissajous scanning grid differently. Hence, the grid can be designed to obtain higher resolution at

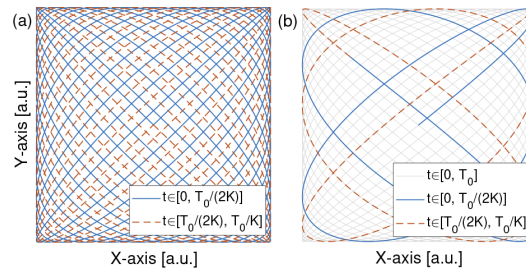


Fig. 2. Examples of Lissajous scan patterns. (a) No preview scanning ($N_{X0} = 26$, $N_{Y0} = 25$, $K = 1$, $f_0 = 90$ Hz). (b) Fast preview scanning due to $K > 1$ ($N_{X0} = 26$, $N_{Y0} = 21$, $K = 5$, $f_0 = 90$ Hz).

desired positions in the field of view, i.e. at regions of interest, without sacrificing the frame rate. As also shown in the figure, the increased resolution at one position is sacrificed with a lower resolution at another position. Furthermore, the scanning grid features defined in one quadrant, e.g. Q1, also appear in the other quadrants due to the symmetry of the Lissajous scanning method.

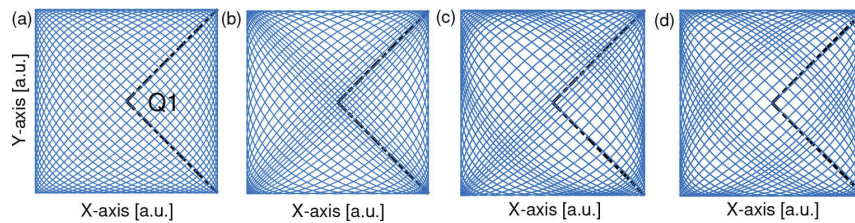


Fig. 3. Examples of adaptive Lissajous scan patterns using single frequency modulation functions Eq. (12): (a) no modulation, (b) only second order $a_2 = 0.25$ rad, (c) only third order $a_3 = 0.15$ rad and (d) only fourth order $a_4 = -0.1$ rad. The Lissajous parameters $N_{X0} = 26$, $N_{Y0} = 25$ and the frame rate are unchanged. Also the similarity quadrant Q1 is shown where the grid features are repeated in the other quadrants.

3.2. Pixel distribution and resolution criterion

For a phase modulation function, design criteria have to be defined to evaluate the resulting scan grid. In this study the resolution is defined by the distance of neighboring pixels, which are derived from scan line intersection points, as this reveals the uncovered area. For simplicity, the intersection points of a Lissajous scan grid without phase modulation is discussed first. With the identity of $\sin(\varphi) = \sin(n\pi + (-1)^n \varphi)$ for any integer number n , the conditions such that two scan lines intersect can be expressed as

$$\begin{aligned} \sin(2\pi f_X t_j) &\stackrel{!}{=} \sin(n_{Xj}\pi + (-1)^{n_{Xj}} 2\pi f_X t_j) \quad \text{and} \\ \sin(2\pi f_Y t_j) &\stackrel{!}{=} \sin\left(n_{Xj}\pi \frac{N_{Y0}}{N_{X0}} + (-1)^{n_{Xj}} 2\pi f_Y t_j\right), \end{aligned} \quad (14)$$

where n_{Xj} is the necessary X-axis half periods shift in between and t_j is the intersection time, which both have to be found for each intersection j . The first condition in Eq. (14) is automatically fulfilled for all times t_j if $n_{Xj} \in \mathbb{Z}$, while only at a certain time also the Y-axis equation is fulfilled.

By sampling the trajectory with the constant sampling time [16]

$$\Delta t_S = \frac{1}{4f_X N_{Y0}}, \quad (15)$$

a high resolution rectilinear pixel grid can be obtained if an initial shift of half a sampling time is applied. It can be found that a subset of the total samples at $t_j = j \Delta t_S$ with the sample number j contains the intersection points, where each is sampled twice along two different scan lines. The subset, which does not belong to intersection points are at the edges of the FoV and correspond to the points where either the X-axis or the Y-axis reaches its amplitude point as shown in Fig. 4. Hence, the total set of samples in one Lissajous period is $S = \{j \in \mathbb{N}_0 \mid 0 \leq j \leq 4N_{Y0}N_{X0} - 1\}$ and the subset $S_I \subset S$ corresponding to intersection points is

$$S_I = \left\{ j \in S \mid \begin{array}{l} j \neq N_{X0}(1 + 2m) \quad \text{and} \\ j \neq N_{Y0}(1 + 2l) \quad \text{with } m, l \in \mathbb{N}_0 \end{array} \right\}. \quad (16)$$

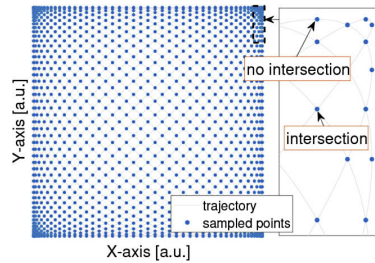


Fig. 4. Obtained samples of the Lissajous trajectory ($N_{X0} = 26$, $N_{Y0} = 25$) with a constant sampling time Δt_S . The samples mainly contain intersection points while also points on the edges of the FoV without an intersection.

In the following, a proof for the intersections happening at the subset S_I of the samples at t_j is derived and subsequently used for phase modulation design. The necessary half period shifts between two intersecting scan lines is first expressed as

$$n_{Xj} = N_{X0} + (-1)^{N_{X0}+j} j \frac{1 - L N_{X0}}{K}, \quad (17)$$

where $L \in \mathbb{N}_0$ has to be chosen such that Eq. (14) is fulfilled. With the equality $f_X N_{Y0} = f_Y N_{X0}$ and Eq. (15), the second equation in Eq. (14) can be rewritten as

$$\sin\left(j \frac{\pi}{2N_{X0}}\right) \stackrel{!}{=} \sin\left(n_{Xj} \pi \frac{N_{Y0}}{N_{X0}} + (-1)^{n_{Xj}} j \frac{\pi}{2N_{X0}}\right) = \sin\left(n_{Yj} \pi + (-1)^{n_{Yj}} j \frac{\pi}{2N_{X0}}\right), \quad (18)$$

where $n_{Yj} \in \mathbb{Z}$ is the corresponding Y-axis half periods shift and can be found to

$$n_{Yj} = N_{Y0} - (-1)^{N_{Y0}+j} j \frac{1 - L N_{Y0}}{K} = n_{Xj} - K - (-1)^{N_{Y0}+j} j L. \quad (19)$$

The intersection condition is fulfilled for all j if L is chosen such that

$$\frac{1 - L N_{X0}}{K} \quad \text{and} \quad \frac{1 - L N_{Y0}}{K} = \frac{1 - L N_{X0}}{K} + L \quad (20)$$

are odd integers. At least one L value can be found for each valid frequency ratio of an even and an odd integer. As K is then always odd, the above conditions reveal that L has to be even and results in the trivial solution $L = 0$ for the case $K = 1$. A proof is given in the [Appendix](#).

Exceptionally the intersection condition with the used expressions is also fulfilled for the subset of the samples which actually are no intersection points, i.e. $S \setminus S_I$. This is because for those samples both X-axis and Y-axis phases are shifted by a multiple of the Lissajous period, i.e. the points intersect with themselves. Hence, those samples do not have to be excluded or separately treated from the algorithm.

By shooting a pulsed laser on the scan lines between two adjacent samples, a rectilinear high resolution pixel grid is obtained. In case of no modulation, this can be accomplished by a simple shift of the sample time t_j by half a sampling time, i.e.

$$t_{px_j} = t_j + \frac{\Delta t_S}{2} = \left(j + \frac{1}{2}\right) \Delta t_S. \quad (21)$$

An example is shown in Fig. 5(a), where the pixels are arranged in horizontal and vertical lines.

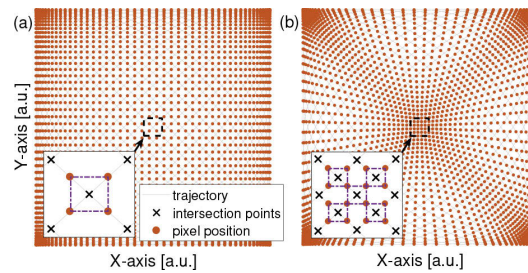


Fig. 5. Examples of pixel distributions and definition of polygon for resolution calculation (dashed rectangles in the insets). (a) No phase modulation, where a rectilinear grid with horizontal and vertical pixel lines is obtained. (b) Second order ($a_2 = 0.25$ rad) phase modulation, where the pixel lines are bent to obtain a high resolution at the center of the FoV.

In case of a modulated Y-axis as in Eq. (7), the intersection points do not happen at a constant sampling time. Hence, the sample times are expressed as

$$t_j = j \Delta t_S + \Delta t_j, \quad (22)$$

where Δt_j has to be identified for all j and the new Y-axis intersection criterion is

$$\begin{aligned} & \sin \left(j \frac{\pi}{2N_{X0}} + 2\pi \bar{f}_Y \Delta t_j + \phi(t_j) \right) \\ & \stackrel{!}{=} \sin \left(n_{Xj} \pi \frac{N_{Y0}}{N_{X0}} + (-1)^{n_{Xj}} \left(j \frac{\pi}{2N_{X0}} + 2\pi \bar{f}_Y \Delta t_j \right) + \phi \left(\frac{n_{Xj}}{2f_X} + (-1)^{n_{Xj}} t_j \right) \right). \end{aligned} \quad (23)$$

As the sampling time shifts are expected much smaller than a half period of the scanner, i.e. $|(-1)^{n_{Xj}} 2\pi \bar{f}_Y \Delta t_j + \phi(t_j)| \ll \pi$, a comparison with Eq. (18) shows that the previous calculation of n_{Xj} and n_{Yj} fulfill the condition up to a small shift in phase. Hence, the shifts Δt_j can be calculated by compensating the residual errors in the arguments of the sine functions, i.e.

$$2\pi \bar{f}_Y \Delta t_j + \phi(t_j) \stackrel{!}{=} (-1)^{n_{Yj}} \left((-1)^{n_{Xj}} 2\pi \bar{f}_Y \Delta t_j + \phi \left(\frac{n_{Xj}}{2f_X} + (-1)^{n_{Xj}} t_j \right) \right), \quad (24)$$

where the sign dependency on n_{Yj} takes into account that the trajectory derivative is the same or different for both intersecting scan lines. Further simplification can be obtained by using the

derived symmetry features of the phase modulation function as well as that n_{Xj} and n_{Yj} are never both odd or both even, i.e.

$$2\pi\bar{f}_Y\Delta t_j + \phi(t_j) \stackrel{!}{=} -2\pi\bar{f}_Y\Delta t_j - \phi\left(\frac{N_{X0}}{2f_X} + j\frac{1-LN_{X0}}{2f_XK} + t_j\right). \quad (25)$$

A proof for the sign dependency elimination of the phase modulation function is given in the [Appendix](#). As ϕ is a nonlinear function, Eq. (25) cannot be analytically solved, while Δt_j can be approximated numerically by iterative refinement, i.e.

$$e = \frac{-1}{4\pi\bar{f}_Y} \left(\phi(\hat{t}_j) + \phi\left(\frac{N_{X0}}{2f_X} + j\frac{1-LN_{X0}}{2f_XK} + \hat{t}_j\right) \right) - \Delta\hat{t}_j, \quad (26)$$

where $\hat{t}_j = j\Delta t_S + \Delta\hat{t}_j$ and e is minimized. Hence, with sufficient iterations the estimated time shifts $\Delta\hat{t}_j$ accurately match the exact solutions Δt_j and can be calculated for each intersection point. Again the samples without an intersection do not have to be excluded as the algorithm results in zero shift for those points.

Similar to the case without modulation, the high resolution pixel grid is obtained by interpolating between two adjacent samples, e.g. by linear interpolation

$$t_{px_j} = \frac{1}{2} (t_j + t_{j+1}). \quad (27)$$

Figure 5(b) shows an example of a resulting pixel grid with phase modulation. The original horizontal and vertical pixel lines in Fig. 5(a) are bent such that a high density of pixels is achieved at a certain position in the FoV, e.g. at the center.

The resolution of the pixel grid can be defined by the area spanned by the four pixels, which surround an intersection point, as illustrated in Fig. 5. Hence, for each intersection point at sampling time t_j the four vertices that define the spanned area can be found at the times

$$\mathbf{t}_{V_j} = \begin{bmatrix} t_{px_j}, & t_{px_j}, & t_{px_{j-1}}, & t_{px_{j-1}} \end{bmatrix}, \quad (28)$$

with $l = \left\{ 2N_{X0}N_{Y0} + (-1)^{N_{X0}+j} j \left(1 + 2N_{Y0} \frac{1-LN_{X0}}{K} \right) \right\} \bmod 4N_{X0}N_{Y0},$

where mod is the modulus operator. The corresponding coordinates describe a polygon in the FoV whose spanned area $F(\mathbf{t}_{V_j})$ relates to the resolution, i.e. a large area corresponds to a low resolution. It has to be noted that the polygons can have various shapes and do not have to be rectangular. Figure 6 shows a contour plot of the resulting spanned area for the case of conventional Lissajous scanning and a second order modulation. As expected, the modulation improves the resolution at the center of the FoV and shifts the low resolution regions towards the edges.

3.3. Compensation of amplitude variation

If no dedicated control is applied, the dynamic response of a scanning system can show an amplitude change if the scanning frequency is varied. Consequently the phase modulation causes variations in the scanning amplitude of the corresponding axis within a Lissajous frame and shifts the intersection points especially where both intersecting scan lines have different amplitude. This leads to a distorted pixel grid if no compensation is applied as shown in Fig. 7(a). To account for the amplitude changes, the frequency dependent amplitude function $A(f)$ is introduced and

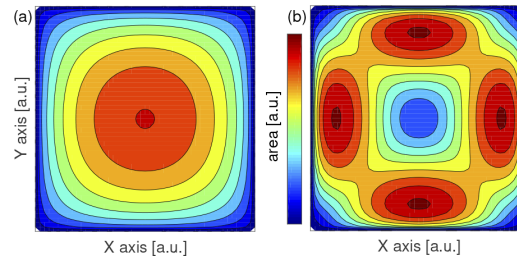


Fig. 6. Contour plot of the area spanned by the four pixels surrounding an intersection point. (a) Conventional Lissajous scanning. The resolution decreases towards the center of FoV. (b) Second order ($a_2 = 0.25$ rad) phase modulation. A high resolution is obtained at the center while other regions are sacrificed.

the trajectory of both axes are described as

$$x(t) = \sin(2\pi f_X t) \quad \text{and} \quad y(t) = A \left(\bar{f}_Y + \frac{1}{2\pi} \dot{\phi}(t) \right) \cdot \sin(2\pi \bar{f}_Y t + \phi(t)). \quad (29)$$

Due to practical usefulness only relatively small amplitude variation can be considered, which only lead to small additive compensation shifts $\Delta t_{A,j}$ of the sample timing, i.e.

$$t_j = j \Delta t_S + \Delta t_j + \Delta t_{A,j}. \quad (30)$$

Hence, $\Delta t_{A,j}$ can be approximated by the Newton-Raphson method applied on the Y-axis trajectory as

$$y(\hat{t}_j) + \dot{y}(\hat{t}_j) e \stackrel{!}{=} y \left(\frac{n_{Xj}}{2f_X} + (-1)^{n_{Xj}} \hat{t}_j \right) + (-1)^{n_{Xj}} \dot{y} \left(\frac{n_{Xj}}{2f_X} + (-1)^{n_{Xj}} \hat{t}_j \right) e, \quad (31)$$

where e has to be zero at the actual intersection point. This leads to the iterative estimation algorithm

$$e = \frac{y \left(\frac{n_{Xj}}{2f_X} + (-1)^{n_{Xj}} \hat{t}_j \right) - y(\hat{t}_j)}{\dot{y}(\hat{t}_j) - (-1)^{n_{Xj}} \dot{y} \left(\frac{n_{Xj}}{2f_X} + (-1)^{n_{Xj}} \hat{t}_j \right)}, \quad (32)$$

where $\hat{t}_j = j \Delta t_S + \Delta t_j + \Delta \hat{t}_{A,j}$ and has to be found to minimize e . Equation (32) can be applied on all samples j except the subset where the Y-axis reaches its amplitude points, i.e. at $j = N_{X0} (1 + 2m)$ with $m \in [0, 2N_{Y0} - 1]$. At those points the trajectory only depends marginally on time and the algorithm is susceptible to numerical errors. Hence, the correct shift should be approximated by interpolating between the previous and the following sample point. Figure 7(b) shows the corrected pixels by the proposed algorithm for an affine amplitude function $A(f) = A_0 (1 + 0.1 (f - \bar{f}_Y) / f_0)$. It has to be noted that no assumptions are made for the amplitude function and it can be an arbitrary function of sufficient smoothness.

3.4. Phase modulation design

Using the derived resolution definition, the phase modulation function can be optimized for specific needs in application. One possibility is to define ROIs, where a high resolution is required while the rest of the FoV is of less interest, i.e. can have reduced resolution. In imaging applications, such as lidar, this allows detailed information where it is required, while still a coarse overall scan is provided. Hence, in this study a dedicated optimization procedure

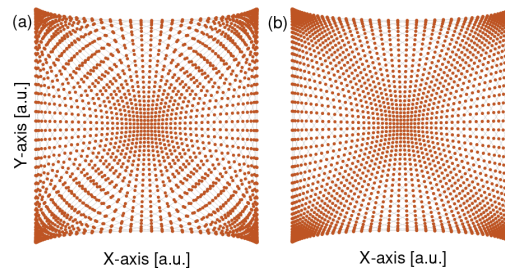


Fig. 7. Examples of pixel distributions for a second order ($a_2 = 0.25$ rad) phase modulation with and without amplitude compensation ($N_{X0} = 26$, $N_{Y0} = 25$, $A(f) = A_0 (1 + 0.1 (f - \bar{f}_Y) / f_0)$). (a) No compensation. (b) Compensation based on the proposed algorithm.

varies the parameters a_i of the phase modulation function to obtain the desired resolution in a defined ROI. To obtain this, the cost function penalizes the resolution at the ROI the most using a spatial weighting. Besides judging the obtained grid resolution solely by the spanned area of neighboring pixels, also its aspect ratio can be taken into account, e.g. to prefer square shaped areas. Furthermore, the dynamic changes of the scanning frequency necessary for the modulation imposes input variations, which depends on the scanner dynamics. As an example, the necessary input amplitudes at the frequency components of the phase modulation function can be considered as a control effort, which might be limited.

The used algorithm can be described in the following steps:

- (i) Calculate the constant Lissajous parameters, such as N_{X0} , N_{Y0} , K , L , n_{Xj} , n_{Yj} (initialization).
- (ii) Choose initial modulation parameters a_i with $1 \leq i \leq M$ for the initial starting point, where M is the maximum order considered for optimization.
- (iii) Calculate sample time shifts $\Delta \hat{t}_j$ and $\Delta \hat{t}_{\Lambda,j}$ according to Eq. (26) and Eq. (32).
- (iv) Calculate cost function terms, e.g. weighted spanned areas, aspect ratios, and control effort. An exemplary cost function is

$$J = \sum_{i=1}^M \underbrace{H_i}_{\text{control effort}} + \sum_{j=0}^{S_I} \underbrace{W(x(t_j), y(t_j))}_{\text{spatial weighting}} \cdot \left[\underbrace{F(\mathbf{t}_{V_j})}_{\text{spanned area}} - \bar{F} \right]^2 \cdot \underbrace{R(\mathbf{t}_{V_j})}_{\text{aspect ratio}}, \quad (33)$$

where \bar{F} is the desired spanned area and $R(\mathbf{t}_{V_j}) \geq 1$ which is equal to 1 for the desired aspect ratio, e.g. for a squared area.

- (v) If the cost function J is not minimum, variation of a_i and jump to (iii).

Figure 8(a)-(b) shows two designs of ROI scan patterns using the proposed optimization procedure and the corresponding phase modulation functions in Fig. 8(c). As can be seen, the straight pixel grid lines of conventional Lissajous scanning are bent to obtain a dense and almost square shaped pixel grid at the ROI. Due to the symmetry of the Lissajous scanning method, the ROI appears similarly in all four quadrants. Figure 9 shows a conceptional illustration of a lidar scenario where the conventional and the proposed Lissajous scanning method are compared. As can be seen, the ROI is resolved with a higher resolution to maximize the information contained

in the measured 3D point cloud, while neither the overall FoV nor the frame rate are sacrificed. In application the computation effort can be minimized by defining a discrete ROI grid in the FoV and to solve the optimization problem for each ROI beforehand. A system controller can then select the appropriate ROI on demand and the corresponding phase modulation function as well as the pixel timings are loaded. This allows fast switching between the ROIs to track objects or to re-scan sacrificed low resolution regions to guarantee that potentially dangerous objects are not missed. A simulation of an object tracking application using discrete ROIs is shown in [Visualization 1](#). The ROI switching speed is then only limited by the ability of the scanner to follow the new modulation function.

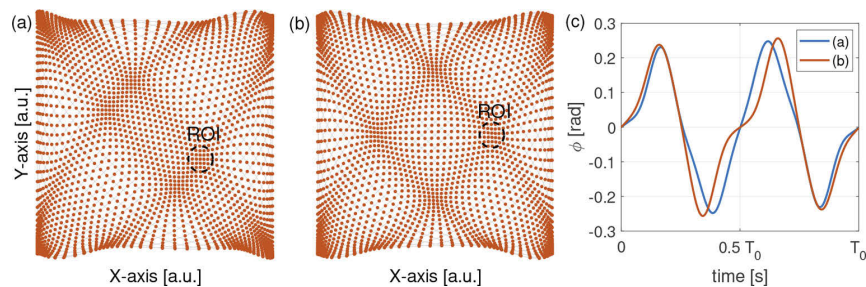


Fig. 8. Examples of ROI scan patterns obtained by the proposed optimization procedure (a-b) and corresponding phase modulation functions (c). The ROI appears in all four quadrants due to the symmetry of Lissajous scanning.



Fig. 9. Conceptual illustration of conventional Lissajous scanning (a) and ROI scanning using the proposed method (b) in a lidar scenario. Significantly more measurement points are created in the ROI compared to the conventional method.

4. Method demonstration

In this section the proposed modulation method is demonstrated by a Lissajous scanning system using two single axis MEMS mirrors with a relatively large frequency tuning capability.

4.1. MEMS mirror

Figure 10 shows a picture of an electrostatic actuated, single axis resonant MEMS mirror and its steady state frequency response. Due to its nonlinear behavior, stable and unstable regions and bifurcation jumps appear in the frequency response as indicated by the arrows. The prominent stiffening, shown by the backbone curve, is caused by a special suspension design using leaf springs and torsion bars. This results in two stable branches in the frequency response, which are called the bottom and the top response curve. The over-bending of the top response curve is advantageously used for the presented method as it provides a rather large frequency band where the amplitude changes are relatively low. This is different from conventional linear resonators, which would require a high damping for a reasonable tuning range, resulting in reduced energy efficiency, i.e. a low Q-factor. Hence, the used MEMS mirrors provide both, a high Q-factor as well as the possibility of frequency variation with a moderate change of amplitude. Around the nominal operation point, the amplitude function $A(f)$ can be approximated as an affine function of frequency as shown in the inset of the figure. A detailed characterization and modeling of a similar MEMS mirror is described in [21].

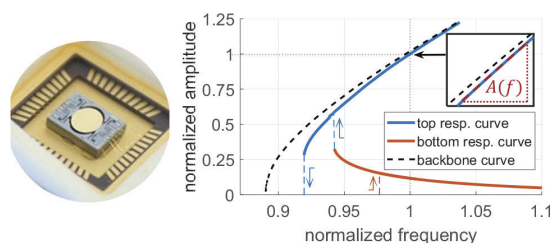


Fig. 10. (left) Picture of the electrostatic actuated resonant MEMS mirrors in a glass covered ceramic package. (right) Measured steady state frequency response, normalized by the nominal operation point. The nonlinearities of the mirror lead to two stable branches, i.e. the bottom and the top response curve. The inset shows a linear relation between amplitude and frequency around the nominal operation point.

4.2. Lissajous scanning system

The Lissajous scanning system comprises two single axis MEMS mirrors of the same type, which are orthogonally oriented to each other as shown in Fig. 11. To obtain the Lissajous scanning pattern, a laser beam is first deflected in Y-axis by the MEMS mirror M1, redirected to the second MEMS mirror M2 by a lens system and deflected in X-axis. A CCD camera monitors the projected pattern on a screen for optical evaluation. A control board provides the driving and sensing circuitry as well as controllers implemented in FPGA to precisely synchronize the mirrors and to perform a desired phase modulation. The detail discussion of control design and implementation can be found in [25].

4.3. Experimental results

To demonstrate the proposed method, the Y-axis MEMS mirror M1 is forced to exhibit a desired phase modulation. Figure 12 shows various ROI scan patterns compared to a conventional Lissajous scan. The bright line in the image is caused by a direct reflection of the first mirror scan line on the second mirror cover class. In application, this can be removed by glass coating or other mirror packaging [26]. Visualization 2 demonstrates the subsequent switching between ROIs, where the corresponding phase modulation functions are calculated beforehand. The transition from one ROI to the next is achieved within about 30 ms. A pixel distribution derived

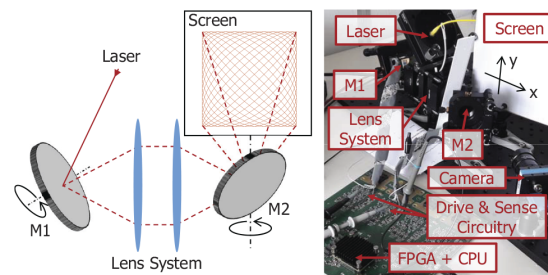


Fig. 11. Scheme (left) and picture (right) of the Lissajous scanning system with two orthogonally oriented single axis MEMS mirrors. Dedicated controllers are implemented in an FPGA, which is configured and monitored by an on-board CPU. For optical evaluation, the generated Lissajous pattern is projected on a screen and monitored by a CCD camera.

by the proposed methods is shown in Fig. 12(e)-(f). The amplitude variations are compensated based on the linear $A(f)$ relation obtained from the frequency response of the mirror, resulting in a proper projection of the desired grid. Insets in the figure show the zoomed center grids for both cases, where the modulated case provides a pixel distance reduced by a factor of 2.25. This results in a resolution improvement by a factor of 5 due to the reduced area spanned by neighboring pixels. As the modulated scanner is limited to a narrow frequency band with a known frequency variation, the controllers are still simple and do not need a high bandwidth.

In summary, the proposed phase modulation method for Lissajous scanning is successfully implemented and several ROI scan patterns are demonstrated. The laser is shot at the correct timing with a compensation of the dynamic amplitude variations. The resulting improved resolution at the center of the FoV demonstrates the capability of the proposed method.

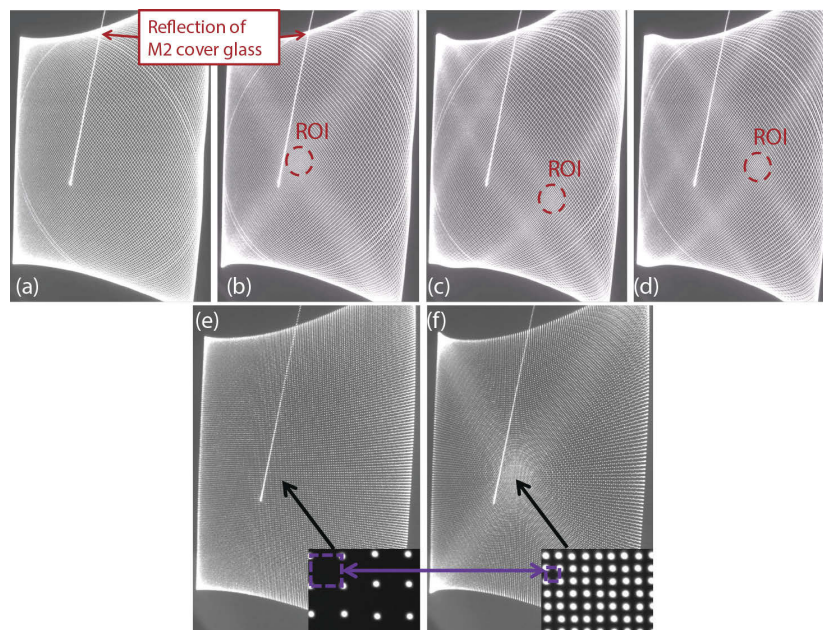


Fig. 12. Adaptive Lissajous pattern examples for ROI scanning. The visible line is a reflection on the cover glass of the second MEMS mirror M2. (a) Conventional Lissajous scan. (b-d) Phase modulation to obtain a desired ROI scan (see [Visualization 2](#)). (e) Conventional pixel distribution. (f) Proposed pixel distribution for a second order modulation. The insets show the pixel grid at the center of the FoV and demonstrate a reduction of the spanned area by a factor of 5 using the proposed modulation method.

5. Conclusion

In accordance to literature the analysis of conventional Lissajous scanning reveal that resolution has to be sacrificed with the frame rate and that the scanning pattern shape is fixed. The proposed method of adaptive Lissajous scanning based on phase modulation provides an additional freedom in the pattern design to overcome this problem. The implementation of the proposed methods in a Lissajous scanning system based on MEMS mirrors demonstrates the feasibility and shows cases of ROI scanning with a local resolution improvement by a factor of 5. The derived constraints of phase modulation reveal that the phase modulation function has to consist of sine waves with frequencies of multiples of the preview frame rate. The proposed pixel timing calculation, shows that the rectilinear grid lines of conventional Lissajous scanning are bent such that a desired ROI has higher pixel density while other regions are sacrificed. A detailed analysis of the scan line intersection points allowed a simple and fast method of resolution calculation based on the spanned area between neighboring pixels over the total FoV. A proposed optimization procedure results in a phase modulation function, which provides the desired scan pattern by judging the obtained resolution, i.e. the spanned area, its aspect ratios as well as the needed control effort due to fast frequency changes.

Appendix

In the following it is proven that

$$n_{Xj}\pi \frac{N_{Y0}}{N_{X0}} + (-1)^{n_{Xj}} j \frac{\pi}{2N_{X0}} = n_{Yj}\pi + (-1)^{n_{Yj}} j \frac{\pi}{2N_{X0}} \quad (34)$$

is fulfilled if L in Eq. (17) and Eq. (19) is an even and $\frac{1-LN_{X0}}{K}$ is an odd integer. Inserting these two conditions into the expressions for n_{Xj} and n_{Yj} yields

$$n_{Xj} = N_{X0} + (-1)^{N_{X0}+j} j \overbrace{\frac{1-LN_{X0}}{K}}^{\text{odd}} \quad \text{and} \quad n_{Yj} = n_{Xj} - K - (-1)^{N_{Y0}+j} j \overbrace{L}^{\text{even}}. \quad (35)$$

With the above equations and $N_{Y0} = N_{X0} - K$, the left and the right hand side in Eq. (34) can be rewritten to

$$-(-1)^{N_{X0}+j} j\pi \left(\frac{1}{N_{X0}} - L \right) + (-1)^{n_{Xj}} j \frac{\pi}{2N_{X0}} = -(-1)^{N_{Y0}+j} j\pi L + (-1)^{n_{Yj}} j \frac{\pi}{2N_{X0}}, \quad (36)$$

where common terms are eliminated. By analyzing Eq. (35) and that either N_{X0} or N_{Y0} is even while the other is odd (K is odd), the exponents in Eq. (36) can be equivalently written as

$$(-1)^{N_{Y0}+j} = -(-1)^{N_{X0}+j}, \quad (-1)^{n_{Yj}} = -(-1)^{n_{Xj}}, \quad \text{and} \quad (-1)^{n_{Xj}} = (-1)^{N_{X0}+j}. \quad (37)$$

Using this equivalences on both sides of Eq. (36) yields

$$-j\pi \left(\frac{1}{N_{X0}} - L \right) + j \frac{\pi}{2N_{X0}} = j\pi L - j \frac{\pi}{2N_{X0}}, \quad (38)$$

which is true and therefore proves the equality of Eq. (34).

The equivalences in Eq. (37) are also used to proof the sign dependency elimination of the phase modulation function in Eq. (25). With the definition of n_{Xj} it can be found that

$$(-1)^{n_{Yj}} \phi \left(\frac{n_{Xj}}{2f_X} + (-1)^{n_{Xj}} t_j \right) = (-1)^{n_{Yj}} \phi \left(\frac{N_{X0}}{2f_X} - (-1)^{n_{Yj}} \left(j \frac{1-LN_{X0}}{2f_X K} + t_j \right) \right). \quad (39)$$

As the phase modulation function is anti-symmetric regarding half a Lissajous period shift, i.e.

$$\phi \left(\frac{N_{X0}}{2f_X} - t \right) = \phi \left(\frac{T_0}{2} - t \right) = -\phi \left(\frac{T_0}{2} + t \right) = -\phi \left(\frac{N_{X0}}{2f_X} + t \right), \quad (40)$$

the sign dependency can be eliminated.

Funding. This work has been supported in part by the Austrian Research Promotion Agency (FFG) under the scope of the AUTOScan project (FFG project number 884345). The authors acknowledge the TU Wien Bibliothek for financial support through its Open Access Funding Program.

Acknowledgments. The authors would like to thank our project partners from Infineon Technologies AG, especially Boris Kirillov, Thomas Thurner, Marcus Hennecke, Stefan Mendel and Leonhard Kormann for fruitful discussions.

Disclosures. The authors declare no conflicts of interest.

Data availability. No data were generated or analyzed in the presented research.

References

1. H. W. Yoo, N. Druml, D. Brunner, C. Schwarzl, T. Thurner, M. Hennecke, and G. Schitter, "MEMS-based lidar for autonomous driving," *Elektrotech. Inftech.* **135**(6), 408–415 (2018).
2. J. Rapp, J. Tachella, Y. Altmann, S. McLaughlin, and V. K. Goyal, "Advances in single-photon lidar for autonomous vehicles: Working principles, challenges, and recent advances," *IEEE Signal Process. Mag.* **37**(4), 62–71 (2020).
3. Z. Tasneem, C. Adhivarahan, D. Wang, H. Xie, K. Dantu, and S. J. Koppal, "Adaptive fovea for scanning depth sensors," *The Int. J. Robotics Res.* **39**(7), 837–855 (2020).
4. J. Wu, Y. Lin, Y. Lo, W. Liu, and L. Fu, "Lissajous hierarchical local scanning to increase the speed of atomic force microscopy," *IEEE Trans. Nanotechnol.* **14**(5), 810–819 (2015).
5. E. Csencsics, S. Ito, J. Schlarp, and G. Schitter, "System integration and control for 3d scanning laser metrology," *IEEE J. Ind. Appl.* **8**(2), 207–217 (2019).
6. P. A. Kirkby, K. M. N. S. Nadella, and R. A. Silver, "A compact acousto-optic lens for 2d and 3d femtosecond based 2-photon microscopy," *Opt. Express* **18**(13), 13720–13744 (2010).
7. K. Nadella, H. Roš, C. Baragli, V. Griffiths, G. Konstantinou, T. Koimtzis, G. Evans, P. Kirkby, and R. Silver, "Random-access scanning microscopy for 3d imaging in awake behaving animals," *Nat. Methods* **13**(12), 1001–1004 (2016).
8. P. F. McManamon, T. A. Dorschner, D. L. Corkum, L. J. Friedman, D. S. Hobbs, M. Holz, S. Liberman, H. Q. Nguyen, D. P. Resler, R. C. Sharp, and E. A. Watson, "Optical phased array technology," *Proc. IEEE* **84**(2), 268–298 (1996).
9. A. C. Lesina, D. Goodwill, E. Bernier, L. Ramunno, and P. Berini, "On the performance of optical phased array technology for beam steering: effect of pixel limitations," *Opt. Express* **28**(21), 31637–31657 (2020).
10. H. W. Yoo, S. Ito, and G. Schitter, "High speed laser scanning microscopy by iterative learning control of a galvanometer scanner," *Control. Eng. Pract.* **50**, 12–21 (2016).
11. A. Bazai, Y. K. Yong, and S. O. R. Moheimani, "High-speed lissajous-scan atomic force microscopy: Scan pattern planning and control design issues," *Rev. Sci. Instrum.* **83**(6), 063701 (2012).
12. K. Hwang, Y.-H. Seo, J. Ahn, P. Kim, and K.-H. Jeong, "Frequency selection rule for high definition and high frame rate lissajous scanning," *Sci. Rep.* **7**(1), 14075 (2017).
13. T. Tuma, J. Lygeros, A. Sebastian, and A. Pantazi, "Analysis and design of multiresolution scan trajectories for high-speed scanning probe microscopy," *IFAC Proc.* **46**(5), 138–144 (2013). 6th IFAC Symposium on Mechatronic Systems
14. Q. A. A. Tanguy, O. Gaiffe, N. Passilly, J.-M. Cote, G. Cabodevila, S. Bargiel, P. Lutz, H. Xie, and C. Gorecki, "Real-time lissajous imaging with a low-voltage 2-axis mems scanner based on electrothermal actuation," *Opt. Express* **28**(6), 8512–8527 (2020).
15. T. Tuma, J. Lygeros, A. Sebastian, and A. Pantazi, "Optimal scan trajectories for high-speed scanning probe microscopy," in *2012 American Control Conference (ACC)*, (2012), pp. 3791–3796.
16. H. Moriguchi, M. Wendt, and J. L. Duerk, "Applying the uniform resampling (urs) algorithm to a lissajous trajectory: Fast image reconstruction with optimal gridding," *Magn. Reson. Med.* **44**(5), 766–781 (2000).
17. Y. Kawai, J.-H. Kim, N. Inomata, and T. Ono, "Parametrically actuated resonant micromirror using stiffness tunable torsional springs," *Sens. Mater.* **28**(2), 131–139 (2016).
18. A. Caspani, C. Comi, A. Corigliano, G. Langfelder, V. Zega, and S. Zerbin, "Dynamic nonlinear behavior of torsional resonators in MEMS," *J. Micromech. Microeng.* **24**(9), 095025 (2014).
19. T. Izawa, T. Sasaki, and K. Hane, "Scanning micro-mirror with an electrostatic spring for compensation of hard-spring nonlinearity," *Micromachines* **8**(8), 240 (2017).
20. T. Sandner, T. Grasshoff, M. Wildenhain, and M. Schwarzenberg, "Hybrid assembled MEMS scanner array with large aperture for fast scanning lidar systems," *Tech. Mess.* **86**(3), 151–163 (2019).
21. D. Brunner, H. W. Yoo, T. Thurner, and G. Schitter, "Data based modelling and identification of nonlinear SDOF MOEMS mirror," *Proc. SPIE* **10931**, 1093117 (2019).
22. W. O. Davis, "Measuring quality factor from a nonlinear frequency response with jump discontinuities," *J. Microelectromech. Syst.* **20**(4), 968–975 (2011).
23. S. Z. Sullivan, R. D. Muir, J. A. Newman, M. S. Carlsen, S. Sreehari, C. Doerge, N. J. Begue, R. M. Everly, C. A. Bouman, and G. J. Simpson, "High frame-rate multichannel beam-scanning microscopy based on lissajous trajectories," *Opt. Express* **22**(20), 24224–24234 (2014).
24. J. Wang, G. Zhang, and Z. You, "Design rules for dense and rapid lissajous scanning," *Microsyst. Nanoeng.* **6**(1), 101 (2020).
25. D. Brunner, H. W. Yoo, R. Schroedter, and G. Schitter, "Modeling and precise synchronization control of parametrically driven resonant mems mirrors," *Mechatronics* p. submitted (2021).
26. U. Hofmann, J. Janes, and H. Quenzer, "High-q MEMS resonators for laser beam scanning displays," *Micromachines* **3**(2), 509–528 (2012).

108.191.204.251 26/08/2021 08:17 02/24/2021